

3.4% Solar-to-Ammonia Efficiency from Nitrate Using Fe Single Atomic Catalyst Supported on MoS₂ Nanosheets

Ji Li, Yuan Zhang, Chao Liu, Lirong Zheng, Eddy Petit, Kun Qi, Yang Zhang, Huali Wu, Wensen Wang, Antoine Tiberj, Xuechuan Wang, Manish Chhowalla, Luc Lajaunie, Ruohan Yu, and Damien Voiry*


Electrochemical synthesis of NH₃ is a carbon-free alternative to the traditional Haber–Bosch process. Obtaining NH₃ from environmental pollutants, such as nitrates or nitrites, is a more practical route than from the nitrogen reduction reaction (NRR) due to the difficult cleavage of the inert triple bond of nitrogen gas. Here, a novel heterogeneous catalyst is reported based on iron (Fe) single-atoms supported on 2D MoS₂ (Fe–MoS₂) for the nitrate reduction reaction (NO₃RR). Fe–MoS₂ exhibits remarkable performance with a maximum Faradaic efficiency of 98% for NO₃RR to NH₃ at an onset potential of –0.48 V versus the reversible hydrogen electrode (RHE) as confirmed by the isotopic nuclear magnetic resonance (NMR) analyses. Density functional theory (DFT) calculations reveal that the enhanced selectivity for the production of NH₃ from single Fe atoms supported on MoS₂ is attributed to a reduced energy barrier of 0.38 eV associated with de-oxidation of *NO to *N. The catalysts are coupled to an InGaP/GaAs/Ge triple-junction solar cell to demonstrate a solar-to-ammonia (STA) conversion efficiency of 3.4% and a yield rate of 510 μg h⁻¹ cm⁻². The results open new avenues for the design of single-atom catalysts (SAC) for the realization of solar-driven ammonia production.

1. Introduction

Ammonia (NH₃) is an important industrial chemical that is widely applied as a nitrogen-rich fertilizer for agriculture, textiles, plastics, and the pharmaceutical industry.^[1,2] The N cycle perturbation is among the 3 identified planetary boundaries that have already been transgressed by humanity.^[3] For renewable energy and net-zero carbon emission, ammonia has been identified as a promising energy carrier because of its high hydrogen content of 17.7 wt.% and its high gravimetric energy density at 3 kWh kg⁻¹.^[4–7] The synthesis of NH₃ via the Haber–Bosch reaction is done under harsh conditions with temperatures and pressures exceeding 400 °C and 200 bar, respectively. With an annual production of 250 × 10⁶ tons, an estimated amount of 1% of the world's energy is utilized in the Haber–Bosch,

J. Li, Y. Zhang, X. Wang
College of Bioresources and Materials Engineering
Shaanxi University of Science & Technology
Xi'an 710021, P. R. China
Y. Zhang, E. Petit, K. Qi, Y. Zhang, H. Wu, W. Wang, D. Voiry
Institut Européen des Membranes
IEM
UMR 5635
Université Montpellier
ENSCM
CNRS
Montpellier, Cedex 5 34095, France
E-mail: damien.voiry@umontpellier.fr
C. Liu
Shaanxi Collaborative Innovation Center of Industrial Auxiliary Chemistry
and Technology
Shaanxi University of Science and Technology
Xi'an 710021, P. R. China
L. Zheng
Institute of High Energy Physics
Chinese Academy of Science
Beijing 100049, P. R. China

A. Tiberj
Laboratoire Charles Coulomb (L2C)
Université de Montpellier
CNRS
Montpellier 34095, France
M. Chhowalla
Department of Materials Science & Metallurgy
University of Cambridge
Cambridge CB3 0FS, UK
L. Lajaunie
Instituto Universitario de Investigación de Microscopía
Electrónica y Materiales (IMEYMAT)
Departamento de Ciencia de los Materiales e Ingeniería
Metalúrgica y Química Inorgánica
Facultad de Ciencias
Universidad de Cádiz
Campus Río San Pedro S/N
Puerto Real, Cádiz 11510, Spain
R. Yu
Nanostructure Research Centre (NRC)
Wuhan University of Technology
Wuhan 430070, P. R. China

 The ORCID identification number(s) for the author(s) of this article can be found under <https://doi.org/10.1002/adfm.202108316>.

DOI: 10.1002/adfm.202108316

which is responsible for 1.4% of the global carbon dioxide emissions.^[8–10] As an alternative, the use of nitrogen and water for the electro-catalytic synthesis of ammonia has recently attracted widespread attention.^[11,12] However, the direct electrochemical reduction of N₂ for the production of ammonia under mild conditions is severely limited by several bottlenecks such as: i) the high energy barrier required for cleavage of inert N≡N triple bond;^[13,14] ii) nonpolar nature of nitrogen molecules that results in a weak interaction between N₂ and active sites of catalysts;^[15] iii) the very low solubility of N₂ in water leading to slow reaction rates.^[16,17]

Alternatively, nitrates (NO₃⁻) possess unique advantages as nitrogen sources for the electrosynthesis of NH₃. The bond energy of polar N=O (204 kJ mol⁻¹) is four times weaker than the inert non-polar N≡N triple bond, and therefore the N=O bond can be easily activated at lower energies.^[18] Nitrate is widely present in the environment and accumulates over time due to agriculture and industrial production activity.^[19,20] NO₃⁻ is a common pollutant of water resources that is responsible for birth defects such as infant methemoglobinemia and blue-baby syndrome as well as thyroid and bladder cancers. NO₃RR for NH₃ production is therefore not only in line with energy sustainability but is also a pollution mitigation strategy. The electrocatalytic reduction of NO₃⁻-to-NH₃ has been reported using Fe,^[21] Al,^[21] Cu bulk and nanorods,^[22,23] Cu₂O/Cu wires,^[24] Cu-Ni alloys,^[25] Cu molecular catalyst,^[17] Co₃O₄,^[26–29] CoP nanoarray,^[30] Ni₂P nanosheets,^[31] single atom Fe,^[32] cobalt nano arrays,^[33] oxide derived cobalt,^[34] and carbon-based materials.^[35,36] Improved current density has recently been obtained from cobalt-based electrodes, but they rely on a high loading amount of cobalt. Conversely, single-atom catalysts (SACs) are anticipated to maximize the atom utilization efficiency of the catalyst but they typically suffer from modest Faradaic efficiencies and/or stability towards the NO₃RR.

We have recently identified chemically exfoliated MoS₂ nanosheets as 2D electrocatalysts for efficient oxidation of organic sulfides to sulfoxides with near-unity selectivity.^[37] The nitrate reductase enzyme possesses a Mo (IV) active site coordinated with sulfur coordinating ligands similar to the dimethyl sulfoxide (DMSO) reductase, whereas the nitrogenase is a multinuclear enzyme with MoFe₇ clusters as the active sites. Fe-based catalysts have been reported to be promising for NO₃RR but the Faradaic efficiency is low because of the competing hydrogen evolution reaction and the formation of nitrogen via the five-electron transfer pathway.^[38–40] To improve the selectivity to NO₃⁻-to-NH₃, Fe SACs hold promise because the individual Fe atoms possess a coordination environment that results in efficient catalytic activity compared to bulk and nanostructured iron. To date, Fe-SACs have been used in various heterogeneous catalytic reactions, such as CO oxidation,^[41] oxygen reduction reaction (ORR),^[42–44] CO₂ reduction reaction (CO₂RR),^[45,46] and nitrogen reduction reaction (NRR).^[47,48]

Inspired by the structure of active sites of enzymes, we report SACs based on individual Fe atoms supported on MoS₂ nanosheets (Fe-MoS₂) for the electrocatalytic NO₃RR, which exhibits excellent performance with a Faradaic efficiency of 98% toward NH₃ at a low overpotential of -0.48 V versus the reversible hydrogen electrode (vs RHE) and a cathodic energy efficiency (EE) of 31% at -0.28 V versus RHE, respectively. The

optimized Fe-MoS₂ SACs were implemented in a 2-electrode electrolyzer coupled to an external photovoltaic (PV) device to allow solar-driven conversion of NO₃⁻ to NH₃ to demonstrate a maximum yield rate of 0.03 μmol h⁻¹ cm⁻² equivalent to 510 μg h⁻¹ with a near-unity FE for NH₃. The system achieved stable ammonia production and we estimated the solar-to-ammonia (STA) conversion efficiency to be ca. 3.4%—setting a new benchmark for the production of NH₃ from a PV-powered electrolyzer based on SACs.

2. Results and Discussion

MoS₂ and Fe-MoS₂ nanosheets were synthesized via a hydrothermal reaction using ammonium tetrathiomolybdate: (NH₄)₂MoS₄ and iron(III) nitrate nonahydrate as precursors of MoS₂ and Fe, respectively.^[49] The morphology of as-synthesized Fe-MoS₂ was characterized by scanning electron microscopy (SEM) and transmission electron microscopy (TEM). TEM and SEM revealed the layered structure of the MoS₂ nanosheets (Figure 1a), cross-sectional TEM revealed the uniform and continuous coverage of the MoS₂ nanosheets film (thickness ≈150 nm) on the conducting carbon cloth (Figure 1b). The High-angle annular dark-field imaging scanning transmission electron microscopy (HAADF-STEM) analysis of single-layer catalyst regions shows that the nanosheets are highly crystalline as evidenced by the fast Fourier transform (FFT) patterns in Figure 1c and Figure S1, Supporting Information. The observation along [110] direction of the MoS₂ slabs reveal the presence of the 1T polytype in Fe-MoS₂ in agreement with the presence of *J* peaks in the Raman spectra (Figure S2, Table S1, Supporting Information). Energy-dispersive X-ray spectroscopy (EDS) elemental mapping was used to confirm the presence of Fe on MoS₂. Figure 1d,e shows uniform distribution of Fe atoms on the nanosheets and no sign of aggregation was observed even at the highest magnification (Figure S3, Supporting Information). The presence of Fe is also highlighted by spatially-resolved electron energy loss spectroscopy (SR-EELS, Figure 1f and Figure S4, Supporting Information). In particular, the EELS chemical maps evidence that the domain size of Fe is equal or below the EELS voxel size (0.16 nm). It should be noted that the presence of oxygen is also highlighted by EELS and will be discussed later. The high-resolution TEM (HR-TEM) images pointed out that Fe-MoS₂ retains the layered structure of MoS₂ with an interlayer distance of ≈ 9.1 Å, ascribed to the (002) crystalline plane (Figure 1g). Compared with pristine MoS₂, the interlayer distance is ≈ 2.8 Å larger in the present samples, which is attributed to the presence of Fe atoms on the surface of the nanosheets (Figure 1g and Figure S5, Supporting Information). This observation is further corroborated by our X-ray diffraction (XRD) analyses in which the *d*-spacing of Fe-MoS₂ was found to be 9.8 Å, which is larger than that of MoS₂ at 6.5 Å (Figure 1h). We studied the influence of Fe atoms on interlayer spacing by preparing Fe-MoS₂ catalysts with increasing loadings from 1.36% to 2.14% (see Supporting Information for details). The position of the (002) did not change significantly with the Fe: Mo ratio suggesting a similar average *d*-space for all Fe-MoS₂ samples. Interestingly the half maximum (FWHM) decreases

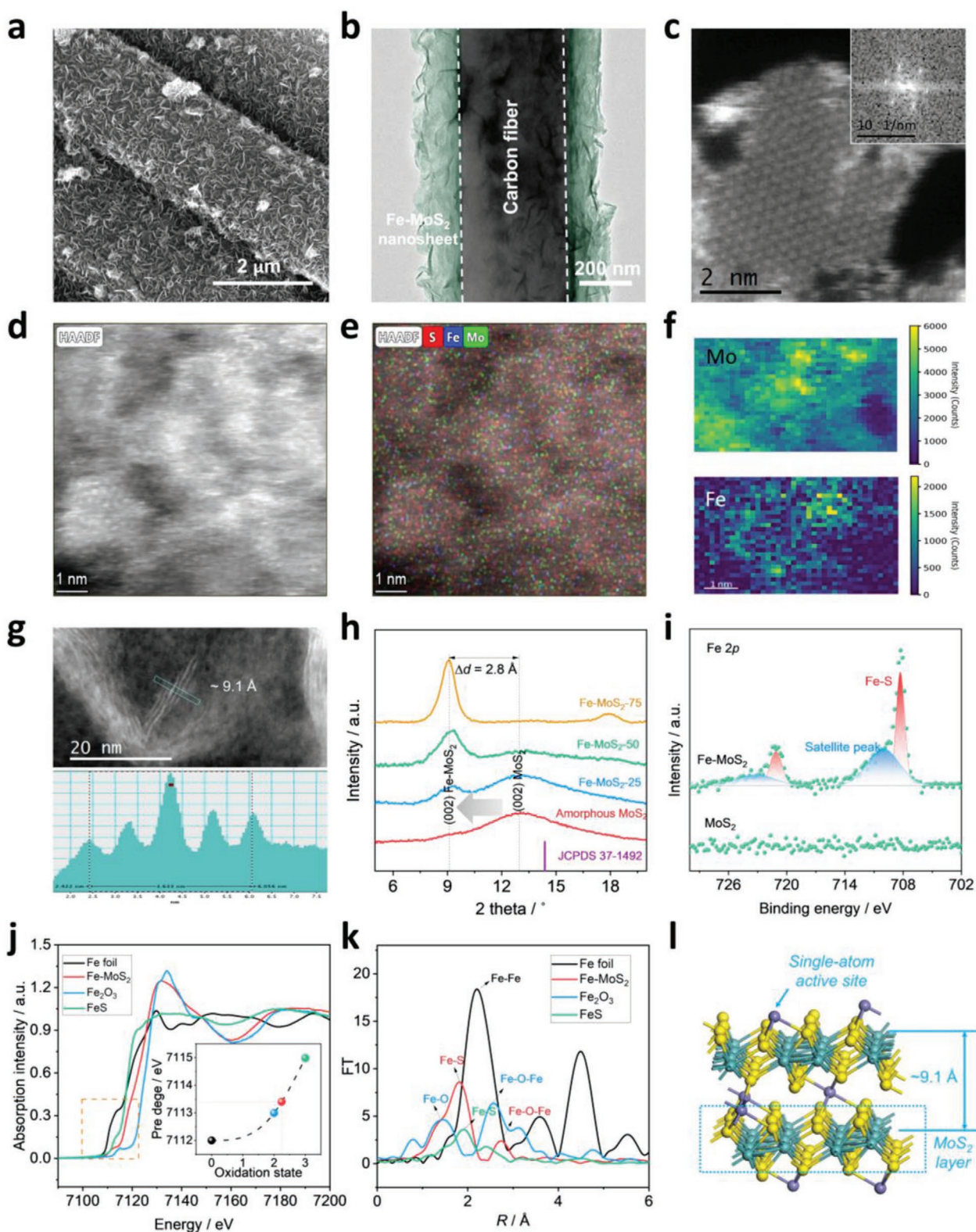


Figure 1. The physical characterizations of Fe-MoS₂. a,b) SEM and TEM images of the Fe-MoS₂ nanosheets grown on the carbon support. c,d) HAADF-STEM image of Fe-MoS₂ nanosheets. Inset: corresponding diffraction pattern confirming the single-crystalline nature of the nanosheet. e,f) High-resolution TEM (HRTEM) - energy dispersive X-ray analyses (EDX) and electron energy loss (EELS) elemental mapping images of Fe-MoS₂ nanosheets. g) HR-STEM image of the interlayer spacing of Fe-MoS₂ and the corresponding line profiles showing an average d-spacing of ≈ 9.1 Å. h) XRD patterns of the Fe-MoS₂ nanosheets with different iron content and compared to pristine MoS₂. i) High resolution Fe2p XPS spectra for Fe-MoS₂ and MoS₂. j) Normalized XANES spectra and k) Fourier transform magnitudes in R space of the EXAFS at the Fe K edge of Fe-MoS₂ nanosheets, Fe₂O₃, FeS, and Fe foil, i) Proposed structure of Fe-MoS₂.

with the Fe content whereas the intensity of the (002) peak increases; indicating improved stacking order and crystallinity of the MoS₂ nanosheets at higher Fe loadings.^[50]

Next, we used X-ray photoelectron spectroscopy (XPS) to elucidate the chemical composition of the MoS₂ and Fe-MoS₂ catalysts. The Fe2p spectra of Fe-MoS₂ unambiguously revealed the presence of Fe on the samples. The spectra can be decomposed into two doublets at 707.9/720.8 and 709.6/723.2 eV, which are ascribed to contributions from Fe bonded to S and the satellite peaks, respectively (Figure 1i).^[51,52] The splitting of the S2p and Mo3d spectra (Figure S6a,b, Supporting Information) for both MoS₂ and Fe-MoS₂ suggests the coexistence of the 1T and the 2H phase MoS₂ in agreement with our Raman and STEM analyses. From the deconvolution of the Mo3d and S2p signals, the amount of 1T phase in MoS₂ and Fe-MoS₂ is estimated to be 42.5% and 47.0% respectively, whereas minimal amount of Mo⁶⁺ is detected at 16.9% and 10.2%. The presence of an additional doublet at 162.6 and 163.9 eV was also identified in the S2p region and attributed to S2p_{1/2} and S2p_{2/3} signals from S–Fe bond.^[53–55] X-ray absorption near-edge spectroscopy (XANES) and extended X-ray absorption fine structure (EXAFS) were acquired to elucidate the electronic and coordination structure of Fe-MoS₂. Figure 1j shows the Fe K-edge XANES profiles for Fe-MoS₂, compared to that of Fe₂O₃, FeS, and Fe metal used as references for Fe³⁺, Fe²⁺, and Fe⁰, respectively. The near-edge absorption energy position of Fe-MoS₂ was found to be between that of FeS and Fe₂O₃, suggesting that the oxidation state of Fe in Fe-MoS₂ is comprised of between +2 and +3. Only one main peak was visible at 1.78 Å in the Fourier transformed EXAFS (FT-EXAFS) spectrum of Fe-MoS₂ (Figure 1k), which is close to that of Fe–S in FeS at 1.87 Å and is attributed to the first coordination shell of Fe–S. It should be noted that no contribution for the Fe–Fe bond expected at ≈2.20 and ≈2.58 Å for Fe⁰ and Fe³⁺ in Fe metal and Fe₂O₃ were observed from the FT-EXAFS spectrum. Our X-ray absorption data suggest the fact that Fe is dispersed on the MoS₂ nanosheets at the atomic level. To gain more information on the structural parameters, we performed least-square EXAFS fittings on Fe-MoS₂ (see Figure S7 and Table S2, Supporting Information). The corresponding coordination number of Fe atom in the Fe-MoS₂ was estimated to be ≈3.5 with the bond lengths of 2.25 and 1.97 Å for Fe–S and Fe–O respectively. The identification of the Fe–O bond may be attributed to the presence of axial oxygen atoms bonded to Fe, in good agreement with the observed spatial overlapping of the Fe and O EELS chemical maps (Figure S4, Supporting Information). All the above results corroborate the single atomic nature of Fe in Fe-MoS₂ catalysts as illustrated in Figure 1l.

The electrocatalytic properties of Fe-MoS₂ catalyst for the reduction of NO₃[−] were investigated in an H-cell reactor using a 0.1 M of Na₂SO₄ + 0.1 M NaOH electrolyte solution (See the Methods section for details about the electrochemical measurements). The left panel of Figure 2a shows linear sweep voltammetry (LSV) curves measured with and without 0.1 M NaNO₃ for Fe-MoS₂. We also compared the electrochemical responses of Fe-MoS₂ nanosheets with MoS₂, Fe foil, carbon cloth used references as well as benchmarked catalysts: Cu, Cu_{0.5}Ni_{0.5}. Higher current density and lower onset potential were detected in the presence of NO₃[−]. To prove that the change in current density originates from the reduction of NO₃[−] to NH₃ rather

than a change in the electrolyte concentration, we estimated the concentration of ammonia after the reaction via a colorimetric method using the indophenol blue method (See details in the Supporting Information file and Figure S8, Supporting Information). Ammonia concentrations were detected in the range of ≈0.6–2.0 mM after 1 h of electrolysis under a constant applied potential of −0.48 V versus RHE, which indicates that the change in the LSV data originates from electrocatalytic conversion of NO₃[−]. To exclude contamination that could lead to overestimation of ammonia production, isotopic experiments were conducted using 0.1 M Na¹⁴NO₃ and 0.1 M Na¹⁵NO₃. The ¹H nuclear magnetic resonance (NMR) spectra of the electrolyte after electrolysis are shown in Figure 2b. In the case of Na¹⁵NO₃ electrolyte solution, the ¹H NMR spectrum exhibits two clear symmetric signals at δ = 7.02 and 7.14 ppm with a spacing of 73.1 Hz assigned to ¹⁵NH₃, due to scalar interaction between ¹H and ¹⁵N. Conversely, in presence of Na¹⁴NO₃ three symmetric signals located at 6.99, 7.08, and 7.17 ppm were detected with a spacing of 52.2 Hz ascribed to ¹⁴NH₃.^[12] We performed a blank experiment in the absence of NO₃[−] and no signals from ¹⁵NH₃ nor ¹⁴NH₃ were detected. Overall, our results confirmed the successful reduction of NO₃[−] to NH₃ and rule out contamination. The content of ammonia in the electrolyte was further quantified via ¹H NMR using an external standard for calibration (Figure S9, Supporting Information). The ammonia quantification using ¹H NMR and colorimetry are comparable and validates our colorimetric strategy for the quantification of the Faradaic efficiency of the reaction on Fe-MoS₂ (Table S4, Supporting Information). Figure 2c shows the Faradaic efficiency for the formation of NH₃ on Fe-MoS₂ compared to pristine MoS₂, Cu, and Cu₅₀Ni₅₀ alloy used as the benchmarked catalyst for the NO₃RR. We noted that Cu, and Cu₅₀Ni₅₀ were prepared and tested according to previous reports from the literature, although we could not achieve the same level of performance.^[25] The selectivity of Fe-MoS₂ nanosheets rapidly increases with the onset potential and the Faradaic efficiency for NH₃ reaches a maximum value of 95.8% at −0.48 V versus RHE, which is higher than that for MoS₂ nanosheets and Cu at 40.8% and 22.5% respectively. We also tested other possible products including NO₂[−], NH₂NH₂, NH₂OH, and N₂ using gas chromatography (GC) and NMR. NH₂NH₂, NH₂OH, and N₂ were not found, while nitrite and hydrogen were detected at low and large overpotentials, respectively (Figure S10, Supporting Information). The enhanced FE on Fe-MoS₂ translates to a specific current density *j*_{NH₃} of −8.4 mA cm^{−2}, which represents 7.1- and 2.8-fold increase compared to MoS₂ and Cu, respectively. The onset potential for NO₃RR—measured at −1 mA cm^{−2}—was found to be ≈ 100 mV versus RHE for Fe-MoS₂, while the absence of Faradaic current below 100 mV versus RHE revealed the absence of electrochemical reactions. For comparison, we determined the onset potential for MoS₂ and Fe to be 200 and 40 mV versus RHE, respectively (Figure 2d). The *j*_{NH₃} and onset potential on Fe-MoS₂ are comparable with those from Cu₅₀Ni₅₀ alloy. To further quantify the catalytic properties of Fe-MoS₂, we estimated the cathodic EE (EE_{NO₃RR}) of the different catalysts. The EE_{NO₃RR} for Fe-MoS₂ was found to be the highest at 31% for a cathodic potential of −0.28 V versus RHE, which is at least 4 times higher than that of MoS₂, Cu, and Cu₅₀Ni₅₀ alloy (Figure 3b). These results also compared favorably with

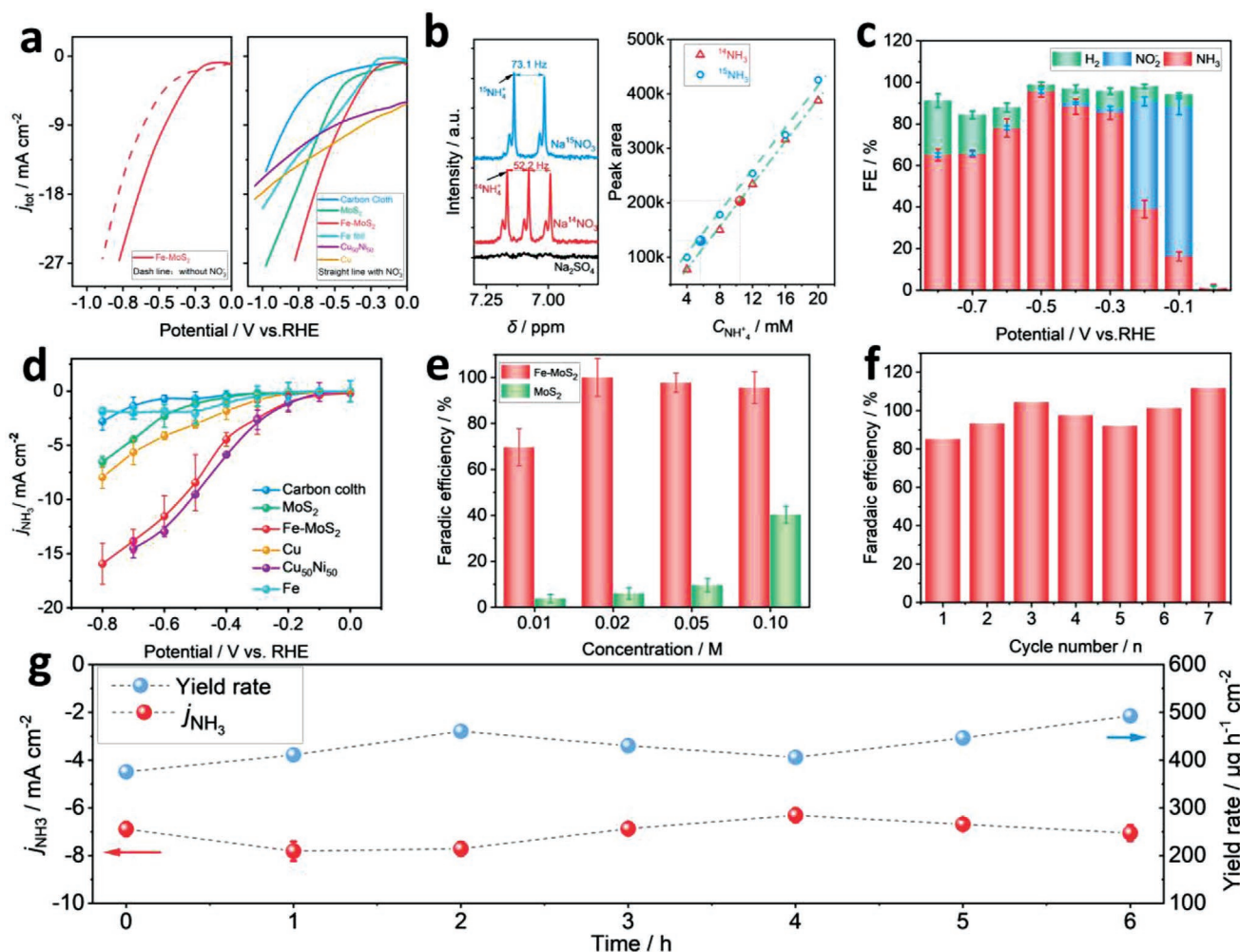


Figure 2. The electrochemical performance investigation for NO₃RR on Fe-MoS₂. a) Left: LSV curves of Fe-MoS₂ nanosheets with and without 0.1 M NaNO₃ electrolyte. Right: LSV curves of Fe-MoS₂ nanosheets, MoS₂ nanosheets, Fe foil, carbon cloth, and benchmarked catalysts: Cu, Cu_{0.5}Ni_{0.5} in presence of 0.1 M NaNO₃. b) Left: ¹H NMR spectra (600 MHz) of electrolyte produced from NO₃RR under −0.58 V versus RHE using 0.1 M Na¹⁴NO₃ and Na¹⁵NO₃ as N source. Right: Calibration curve of ¹⁴NH₄Cl and ¹⁵NH₄Cl measured by ¹H NMR (right). The experimental NO₃RR results are shown as solid symbols. c) Potential-dependent Faradaic efficiency of ammonia on Fe-MoS₂, MoS₂, Cu, Fe foil, compared with the carbon support. d) Evolution of the specific current density: j_{NH_3} as a function of the potential (vs RHE). e) Comparison of the Faradaic efficiency for ammonia on the Fe-MoS₂ and MoS₂ nanosheets at different nitrate concentrations measured at an applied potential of −0.48 V versus RHE. f) Evolution of the Faradaic efficiency at −0.48 V over 7 cycles of 1 h. The electrolyte was refreshed for every cycle. g) Evolution of j_{NH_3} and the yield rate of Fe-MoS₂ nanosheets over time.

previous reports from the literature based on CuNi alloy,^[56] Cu nanosheets,^[57] Cu/CuO nanowire arrays,^[58] titanium electrode,^[59] and copper-molecular solid catalyst (Table S5, Supporting Information),^[17] and other MoS₂-based catalysts those we synthesized (Figure S11, Supporting Information). Our investigations indicate that the presence of atomically dispersed Fe on the 2D MoS₂ matrix enhances both the intrinsic catalytic activity and the selectivity with respect to H₂.

We then sought to better understand the behavior of Fe-MoS₂ by exploring the influence of Fe loading and the nitrate concentration in the electrolyte. At −0.48 V versus RHE, the Faradaic efficiency continuously increases from 30.1% up to 95.8% as the Fe content is increased from 0% (i.e., pristine MoS₂) to 2.13% (Figure S12a,b, Supporting Information). The effect of nitrate concentration on catalytic properties was explored by varying the NO₃[−] concentration from 10 mM up

to 100 mM. Remarkably we observed that the FE for NH₃ on Fe-MoS₂ is largely maintained in presence of diluted NO₃[−] and the FE remains as high as 70% for a nitrate concentration as low as 10 mM. On the contrary, the concentration profoundly affects the NO₃RR performance of MoS₂ and the FE decreases to ≈3.8% for a nitrate concentration of 10 mM (Figure 2e). This apparent 18-fold increase of FE_{NH₃} in dilute medium highlights the high selectivity of Fe-MoS₂ towards the NO₃RR versus the competing hydrogen evolution reaction (HER).

We assessed the charge transfer resistance (R_{CT}) at the interface between Fe-MoS₂ and the electrolyte using electrochemical impedance spectroscopy (EIS) (Figure S13a, Supporting Information). The Nyquist plots of different catalysts exhibit the typical semicircle shape, which reflects the interface resistance on the electrode surface. By modeling the EIS responses with the Randles equivalent circuit, the values of R_{CT} are found to be low

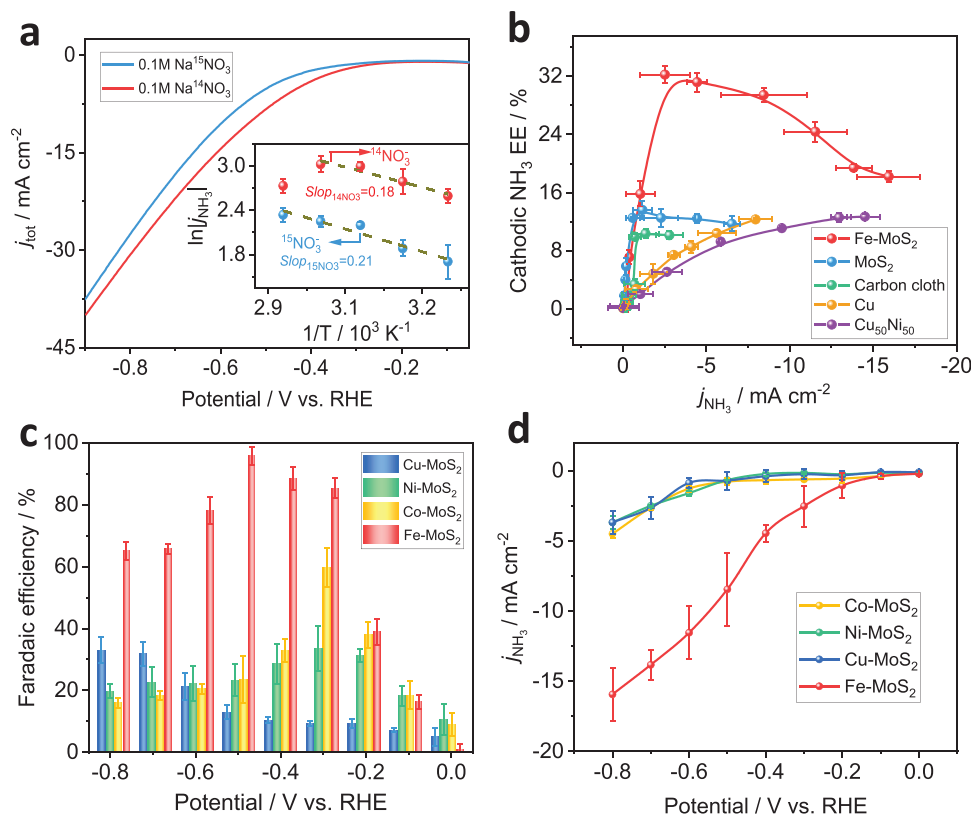


Figure 3. The electrochemical performance towards NO_3RR on MoS_2 -based SACs. a) Linear sweep voltammetry (LSV) and Arrhenius plots (inset) of Fe-MoS_2 measured in $\text{Na}^{14}\text{NO}_3$ and $\text{Na}^{15}\text{NO}_3$ at different temperatures. b) The cathodic EE for NO_3^- -to- NH_3 conversion on Fe-MoS_2 and MoS_2 nanosheets compared with Cu , $\text{Cu}_{50}\text{Ni}_{50}$, and the carbon support. c) Potential-dependent Faradaic efficiency for ammonia on Cu-MoS_2 , Ni-MoS_2 , Co-MoS_2 , and Fe-MoS_2 nanosheets. d) Evolution of j_{NH_3} on Co-MoS_2 , Ni-MoS_2 , and Fe-MoS_2 nanosheets as a function of the applied potential.

in the case of Fe-MoS_2 at 13.1Ω compared to 24.8Ω for MoS_2 and 9.8Ω for Cu . This points to faster kinetics for electron transfer at the surface of the catalyst in agreement with the reduction of the Tafel slope at 260 mV dec^{-1} compared to $>500 \text{ mV dec}^{-1}$ for pristine MoS_2 and other Cu -based catalysts (Figure S13b, Supporting Information). We conclude that the reduced R_{CT} and Tafel slope result from improved conductivity of the Fe-MoS_2 nanosheets and the presence of the metallic 1T polytype within the MoS_2 lattice. To evaluate the stability toward the conversion of NO_3^- to NH_3 , we applied a steady-state potential on the Fe-MoS_2 electrode, while recording the current density and measuring the FE using colorimetry. Figure 2f shows that the FE at -0.48 V versus RHE displays minimal changes over 7 h with an average value of 98%. The robustness of the Fe-MoS_2 performance was further corroborated by the high retention of the current density, showing that the 7-h average of yield rate was $431.8 \pm 38.6 \mu\text{g h}^{-1} \text{ cm}^{-2}$. Finally, to confirm the stability of the Fe single atoms, we measured the content in Fe in the electrolyte after 6 cycles of 1 h of electrolysis. The Fe concentration was found to be below the detection limit of 2 ppb, suggesting limited leaching of Fe atoms during NO_3RR (Table S6, Supporting Information).

We explored the isotopic effect on the NO_3RR by investigating the electrochemical responses of Fe-MoS_2 in presence of $\text{Na}^{14}\text{NO}_3$ and $\text{Na}^{15}\text{NO}_3$ respectively.^[60] Using $\text{Na}^{15}\text{NO}_3$, we observe a decrease in the current density together with an increase of the overpotential of $\approx 40 \text{ mV}$ (Figure 3a). The LSV

and chronoamperometry responses were recorded for each nitrate isotope with increasing temperatures from 25 to $65 \text{ }^\circ\text{C}$ and the apparent activation energies were obtained by fitting the Arrhenius plot of the specific current density j_{NH_3} as a function of T^{-1} (inset Figure 3a). The slope of the Arrhenius plot was estimated to be 0.18 and 0.21 for $\text{Na}^{14}\text{NO}_3$ and $\text{Na}^{15}\text{NO}_3$ respectively. The apparent difference between the two isotopes is in agreement with the change in the polarization curves and is attributed to the slow diffusion of $\text{Na}^{15}\text{NO}_3$ in the Helmholtz layer as well as in the interlayer of Fe-MoS_2 nanosheets.

To obtain more insight into the remarkable selectivity of the Fe-MoS_2 for the electrosynthesis of NH_3 , we investigated NO_3RR on different MoS_2 -based SACs with different transition metals. Figure S14, Supporting Information, shows the polarization curves on Co-MoS_2 , Ni-MoS_2 , Cu-MoS_2 , and Fe-MoS_2 nanosheets in the presence of NO_3^- . Fe-MoS_2 outperformed the other MoS_2 SACs as evidenced by the larger current density and the lower onset potential compared to Co-MoS_2 , Ni-MoS_2 , and Cu-MoS_2 . The FE for NH_3 was found to be 59.6% at -0.3 V versus RHE on Co-MoS_2 , which is lower than that of Fe-MoS_2 at 86.4% (Figure 3c). Remarkably the values of the onset potential for NO_3RR and j_{NH_3} on Fe-MoS_2 are also \approx four-tenfolds higher and at least 400 mV versus RHE lower than other MoS_2 catalysts (Figure 3d)—strongly suggesting that the dispersed Fe atoms on the MoS_2 nanosheets are key for enhancing the intrinsic catalytic activity and selectivity towards the NO_3RR .

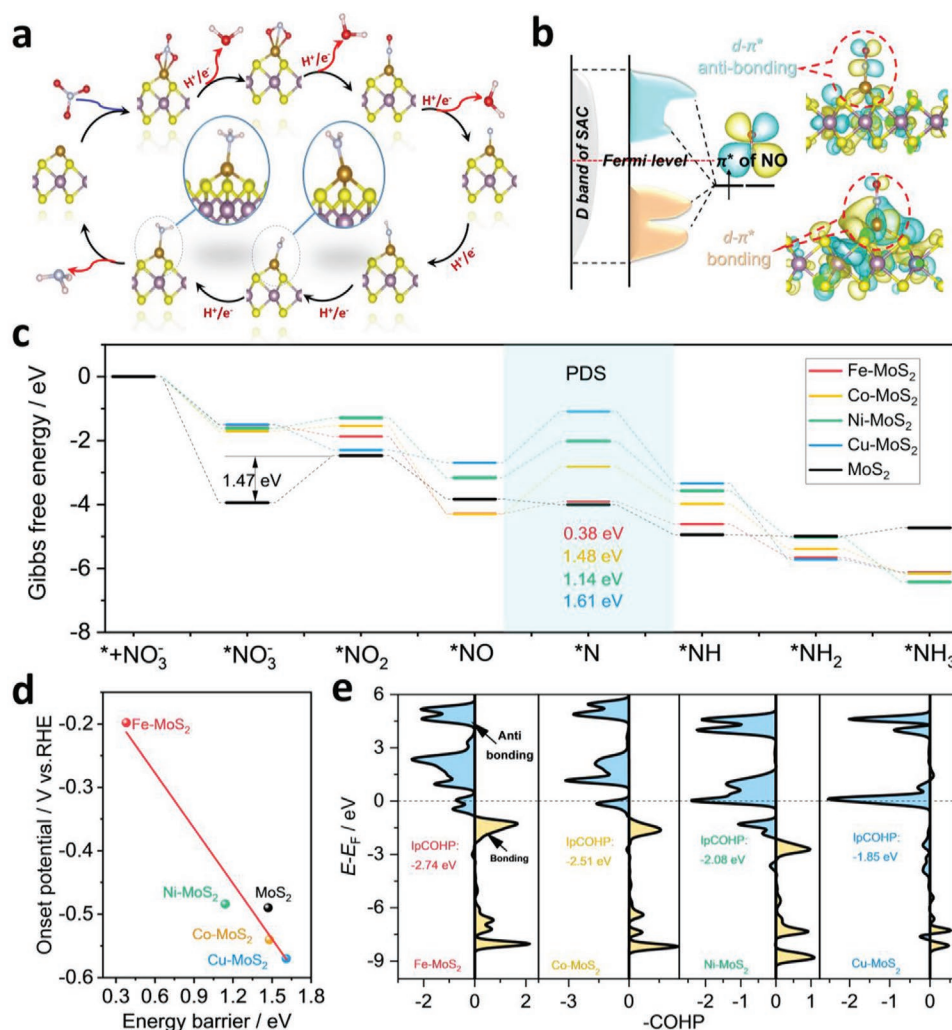


Figure 4. DFT calculations of the NO₃RR on MoS₂ SACs. a) Reaction pathway for the NO₃RR on M-MoS₂ nanosheets (M: Fe, Co, Ni, and Cu, respectively). b) Schematic diagram of the interaction between NO and the M-MoS₂ nanosheets. c) Reaction Gibbs free energies for different intermediates on M-MoS₂ nanosheets. d) Scaling relationship between energy barrier and onset potential of NO₃RR for pristine MoS₂ and M-MoS₂. e) Projected crystal orbital Hamiltonian population (pCOHP) of NO adsorbed on M-MoS₂ nanosheets.

To rationalize our experimental results, we conducted density functional theory (DFT) calculations to investigate the NO₃RR on the different SACs supported on MoS₂. The structural models of SACs consisted of four different transition metals: Fe, Co, Ni, and Cu atoms coordinated with 3 sulfur atoms as presented in Figure S15, Supporting Information.^[61] **Figure 4a** shows the successive steps associated with nitrate reduction on the MoS₂ SACs, which can be decomposed into two main electrochemical processes: *NO₃⁻ → *NO₂ → *NO → *N and *NH → *NH₂ → *NH₃ corresponding to the deoxidation and hydrogenation mechanisms, respectively.^[23,62] There is a general agreement that the catalytic active sites of MoS₂ are located at the edges of the nanosheets.^[63] We first computed the Gibbs free energy of the full NO₃RR pathway on different MoS₂ SACs. On pristine MoS₂, the first deoxidation step: *NO₃⁻ → *NO₂ is considered as the potential-dependent step (PDS) with a very high reaction free energy of 1.47 eV. Such a high value is attributed to the formation of strong covalent bonds between two adjacent Mo atoms and two oxygen atoms of NO₃⁻ (with ΔE_{NO₃⁻} = -4.04 eV

for the largest charge transfer of 0.85 e⁻) (Figure S16, Supporting Information). Conversely, all SACs display a different energy profile illustrating that the inclusion of metallic single atoms profoundly modifies the thermodynamics landscape of the NO₃RR on MoS₂. The PDS step is associated with the *NO deoxidation step (see Figure 4c). Among the different metal single atoms, the lowest reaction free energy is obtained for Fe-MoS₂ at 0.38 eV—in qualitative agreement with our experimental observations. When plotting the energy barrier for the reaction as a function of the experimental onset potential, we observed a linear relationship, which clearly suggests that the catalytic activity of MoS₂ SACs is controlled by the barrier of the deoxidation step (Figure 4d). To confirm the high selectivity towards the formation of ammonia, we calculated the energy profiles for the formation of NO₂, NO, N₂O, and N₂ on Fe-MoS₂. According to our DFT predictions, the energy barrier associated with the formation of NO₂, NO, N₂O, and N₂ are estimated to be 2.01, 3.05, 0.82, and 0.70 eV respectively (Figure S17, Supporting Information). These values are clearly larger than the

barrier associated with the formation of NH_3 , which suggests a high selectivity towards the formation of ammonia on Fe-MoS₂ in agreement with our experimental data.

To elucidate the origin of the reduced energy barrier for the PDS on the active sites, we examined the projected densities of states (PDOS) of NO adsorption on Fe-MoS₂ (Figure S18, Supporting Information). We found that there is a strong overlap between energy levels of the α -spin and β -spin d orbitals of Fe-MoS₂ and the $2\pi^*$ orbitals of NO, which leads to an orbital splitting and rearrangement to form new $d-\pi^*$ bonding and antibonding orbitals (Figure 4b). According to our calculations of the adsorption energy of *NO on the MoS₂ SACs ($E_{\text{ads, NO}}$), we identified the following trend: $E_{\text{ads, NO}}(\text{Fe-MoS}_2) > E_{\text{ads, NO}}(\text{Co-MoS}_2) > E_{\text{ads, NO}}(\text{Ni-MoS}_2) > E_{\text{ads, NO}}(\text{Cu-MoS}_2)$ (Figure S19 and Table S8, Supporting Information). Our results suggest that the stabilization of *NO on Fe-MoS₂ enhances the catalytic activity—in agreement with the Brønsted–Evans–Polanyi (BEP) relation that has been proposed to describe multi-step processes (see Supporting Information). To visualize the bonding situations between the active site and the N atom of NO, we employed the Crystal Orbital Hamiltonian Populations (COHP) analysis,^[64,65] which is a theoretical method for partitioning the band-structure energy into orbital-pair interactions. The integrated projected COHP (IpCOHP) below the Fermi level provides a qualitative estimation of the bond strength. Usually, the bonding state is characterized by a positive overlap population that leads to negative Hamiltonian off-site elements

that contribute to increasing the interactions between adsorbates and the catalyst surface. A comparison of the COHP curves for the four different catalysts (as seen in Figure 4e) reveals that a significant number of antibonding states of M–N interactions (with M and N being the transition metal atom and the N atom in NO) are below the Fermi level of the Ni-MoS₂ and Cu-MoS₂. Conversely, fewer antibonding states of M–N are present below the Fermi levels of the Fe-MoS₂ and Co-MoS₂, which indicates that there is a larger orbital overlap between the d band of the catalyst and the $2\pi^*$ of *NO and a lower electron density in the antibonding orbitals below the Fermi level in both Fe-MoS₂ and the Co-MoS₂. The IpCOHP between Fe and N for Fe-MoS₂ was found to be -2.74 eV more negative than the other three MoS₂ SACs suggesting that stabilization of *NO intermediate is responsible for the reduction of the barrier for the formation of the *N intermediate associated with the PDS step of the reaction.

To evaluate the potential of Fe-MoS₂ for practical ammonia production devices, we integrated the catalysts in a two-electrode H-cell reactor powered by an external PV cell. Figure 5a shows the respective polarization curves of the cathode and the anode measured in a 3-electrode configuration. The onset potentials for the NO₃RR and OER—measured by definition at 1 mA cm² were estimated to be -0.13 and 2.06 V versus RHE, respectively, giving an onset potential of 2.2 V for the full cell. Figure 5b presents the electrocatalytic response of the electrolyzer for applied potentials between 0 to 5.0 without

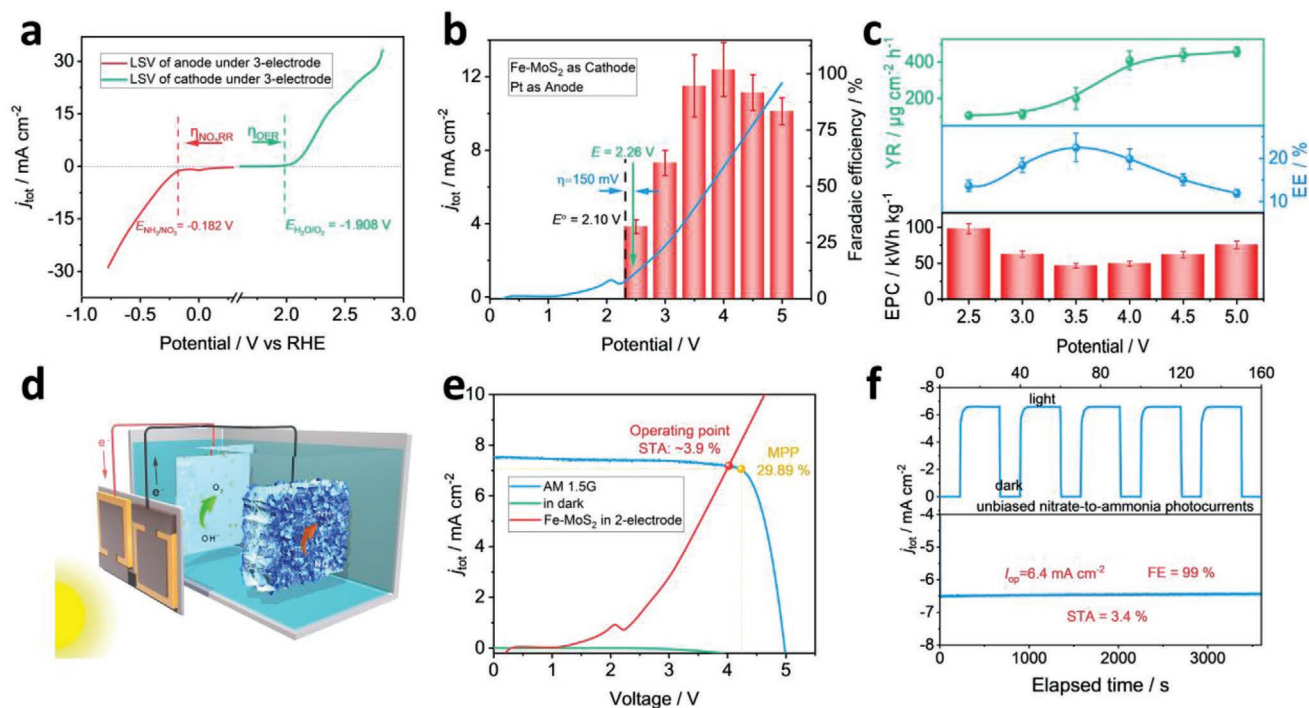


Figure 5. The performance of Fe-MoS₂ for NO₃RR using a 2-electrode electrolyzer. a) LSV curves of Fe-MoS₂ nanosheets and Pt used as a cathode and anode. The LSV responses were measured in a 3-electrode configuration. b) Polarization curve of the full cell electrolyzer with a total geometric area of 2 cm². c) Potential-dependent electric power consumption of ammonia, yield rate, and energetic conversion efficiency of the full-cell device. d) Schematic of the PV-electrolysis system for the conversion of nitrate to ammonia. e) J - V characteristics of the triple junction solar under dark and simulated AM 1.5G 100 mW cm⁻² illumination. Polarization curves of the full cell device based on Fe-MoS₂ nanosheets as NO₃RR catalyst at the cathode. f) Top: Current density–time curve of the PV-EC system without external bias under chopped simulated AM 1.5G 100 mW cm⁻² illumination. Bottom: Stability of the photocatalytic current over 1 h.

compensating for internal resistance. The 2-electrode electrolyzer exhibited an onset potential of 2.26 V consistent with the value predicted from our 3-electrode experiments. We then evaluated the electrolysis property of the full cell, while the Faradaic efficiency was systematically measured at increasing cell voltage. The Faradaic efficiency for NH_3 continuously increased up to 4 V to approach a near-unity value. Figure 5c,d summarizes the full cell EE, the yield rate, EPC, and the electric power consumption (EPC, in kWh kg^{-1}) obtained by varying the voltage. The $\text{EE}_{\text{full-cell}}$ was estimated to be 24.2%, which indicates that our Fe-MoS₂ nanosheets possess a high conversion capability from electric to chemical energy. In addition, the EPC was found to be 46.6 kWh kg^{-1} at 4.0 V while the yield rate reaches a value of 0.024 $\text{mmol h}^{-1} \text{cm}^{-2}$ equivalent to 412.6 $\mu\text{g h}^{-1} \text{cm}^{-2}$. We coupled the 2-electrode H-cell reactor with a PV cell to achieve indirect photocatalytic conversion of nitrate to ammonia. The relatively large potential associated with the electrochemical synthesis of ammonia typically makes the combination of PV and electrolysis processes difficult to realize experimentally at reasonable efficiencies. A GaInAs/Ga(In)As/Ge triple-junction solar cell was used to generate sufficient photovoltage to drive the catalytic reaction. As presented in Figure 5d and Figure S20, Supporting Information, the negative and positive poles were connected with wires to the Fe-MoS₂ cathode and Pt anodes, respectively, and the solar cell was illuminated by standard AM 1.5G spectrum (100 mW cm^{-2}) provided by a Xe solar simulator. Figure 5e presents the J–V characteristic curve of the tandem cell under 1 sun, yielding a V_{OC} of $\approx 5 \text{ V}$ while exhibiting a solar-to-electric power conversion efficiency (PCE) of 29.89%. To accurately calculate the STA conversion efficiency, the LSV curve of the full cell was measured. The size of the electrodes was adjusted in order to minimize the energy loss of the PV-driven electrolysis. We estimated the energy loss between the PV and the PV-electrolysis systems to be only 4.25% (Figure S21, Supporting Information). The operating point was determined from the intersection of the J–V curves of both the solar cell and the H-cell reactor.^[66] The results show that the current density and the cell tension at the operating point reached $\approx 7.19 \text{ mA cm}^{-2}$ and 4.02 V respectively as shown by the red point in Figure 5e. Using the thermodynamic potential of the reaction, the electrolysis current, and the Faradaic efficiency (See Supporting information for details about the calculations), we estimated the solar-to-ammonia (STA) efficiency to be $\approx 3.9\%$. To confirm the accuracy of the predicted operating point, we also measured the photocurrents from the NO₃RR process in an unbiased light-driven configuration (Figure 5f). The operating point of the NO₃RR was close to the maximum power point of the solar panel tandem cell (7.06 mA cm^{-2} at $V_{\text{MP}} = 4.23 \text{ V}$) (the orange point in Figure 5e). We performed solar-driven electrolysis of nitrate for 1 h and the amount of NH_3 was estimated to reach 60.7 μmol ; equivalent to a concentration of 1.02 mM or 173 ppm—larger the contamination threshold of $\approx 1 \text{ ppm}$.^[12] The photocatalytic activity corresponds to a yield rate of $\approx 0.03 \text{ mmol h}^{-1} \text{cm}^{-2}$, equivalent to 510 $\mu\text{g h}^{-1} \text{cm}^{-2}$, which outperforms the previous report on the photocatalysis of the NO₃RR. The estimated STA efficiency was found to be $\approx 3.4\%$, which is among the highest ever reported and sets a new benchmark for solar-driven ammonia production based on SACs (Table S9, Supporting Information).^[34]

3. Conclusion

In summary, we have designed a Fe single-atomic catalyst on 2D MoS₂ nanosheets for electrocatalytic conversion of nitrate to ammonia. Fe-MoS₂ catalysts exhibit excellent NO₃RR properties with Faradaic efficiency as high as 98% for production of NH_3 at a low overpotential of $< -0.5 \text{ V}$ versus RHE and a cathodic EE of 31% at -0.28 V versus RHE. The excellent activity and selectivity of Fe-MoS₂ are supported by DFT analysis, which confirmed the superior ability of individual Fe atoms on MoS₂ to activate NO₃[−] due to the strong interaction between $2\pi^*$ orbital of NO species and *d* band orbitals of Fe atoms that leads to low energy barrier for the limiting *NO to *N reaction. We integrated Fe-MoS₂ in a two-electrode H cell reactor coupled to a PV cell and achieved a STA conversion efficiency of ca. 3.4% with a yield rate of 510 $\mu\text{g h}^{-1} \text{cm}^{-2}$. Our investigation sheds light on a practical strategy for the realization of PV-electrolysis systems for the production of ammonia and opens up future applications for solar-driven NH_3 production.

Supporting Information

Supporting Information is available from the Wiley Online Library or from the author.

Acknowledgements

D.V. acknowledges funding from the European Research Council (ERC) under the European Union's Horizon 2020 research and innovation program (grant agreement No 804320). The authors acknowledge the use of TEM instrumentation provided by the National Facility ELEMIC ICTS ("Division de Microscopia Electronica", Universidad de Cadiz, DME-UCA). L.L. acknowledges funding from the Andalusian regional government (FEDER-UCA-18-106613), the European Union's Horizon 2020 research and innovation program (grant agreement 823 717 – ESTEEM3), and the Spanish Ministerio de Economía y Competitividad (PID2019-107578GA-I00). J.L. acknowledges financial support from the National Science Foundation of China (Grant No. 21 808 134) and start-up funding from Shaanxi University of Science & Technology. This work was supported by the Fundamental Research Funds for the Central Universities (WUT: 2019III012GX, 2020III002GX). Part of the S/TEM investigations was performed at the Nanostructure Research Center (NRC), which was supported by the State Key Laboratory of Advanced Technology for Materials Synthesis and Processing, and the State Key Laboratory of Silicate Materials for Architectures (all of the laboratories are at the Wuhan University of Technology). The authors also acknowledge the use of (S)TEM instrumentation provided by the National Facility ELEMIC ICTS ("Division de Microscopia Electronica", Universidad de Cadiz, DME-UCA).

Conflict of Interest

The authors declare no conflict of interest.

Data Availability Statement

The data that support the findings of this study are available in the supplementary material of this article.

Keywords

ammonia production, electrocatalysis, Fe single-atom catalyst, MoS₂ nanosheets

Received: August 20, 2021
Revised: December 1, 2021
Published online:

- [1] V. Rosca, M. Duca, M. T. de Groot, M. T. M. Koper, *Chem. Rev.* **2009**, *109*, 2209.
- [2] W. Guo, K. Zhang, Z. Liang, R. Zou, Q. Xu, *Chem. Soc. Rev.* **2019**, *48*, 5658.
- [3] W. Steffen, K. Richardson, J. Rockström, S. E. Cornell, I. Fetzer, E. M. Bennett, R. Biggs, S. R. Carpenter, W. De Vries, C. A. De Wit, C. Folke, D. Gerten, J. Heinke, G. M. Mace, L. M. Persson, V. Ramanathan, B. Reyers, S. Sörlin, *Science* **2015**, *347*, 6223.
- [4] R. Schlögl, *Angew. Chem., Int. Ed.* **2003**, *42*, 2004.
- [5] M. D. Fryzuk, *Nature* **2004**, *427*, 498.
- [6] J. Guo, P. Chen, *Chem* **2017**, *3*, 709.
- [7] C. He, Z. Y. Wu, L. Zhao, M. Ming, Y. Zhang, Y. Yi, J. S. Hu, *ACS Catal.* **2019**, *9*, 7311.
- [8] X. Chen, N. Li, Z. Kong, W.-J. Ong, X. Zhao, *Mater. Horiz.* **2018**, *5*, 9.
- [9] I. Rafiqul, C. Weber, B. Lehmann, A. Voss, *Energy* **2005**, *30*, 2487.
- [10] D. Bao, Q. Zhang, F. L. Meng, H. X. Zhong, M. M. Shi, Y. Zhang, J. M. Yan, Q. Jiang, X. B. Zhang, *Adv. Mater.* **2017**, *29*, 1604799.
- [11] Y. Luo, G. F. Chen, L. Ding, X. Chen, L. X. Ding, H. Wang, *Joule* **2019**, *3*, 279.
- [12] S. Z. Andersen, V. Čolić, S. Yang, J. A. Schwalbe, A. C. Nielander, J. M. McEnaney, K. Enemark-Rasmussen, J. G. Baker, A. R. Singh, B. A. Rohr, M. J. Statt, S. J. Blair, S. Mezzavilla, J. Kibsgaard, P. C. K. Vesborg, M. Cargnello, S. F. Bent, T. F. Jaramillo, I. E. L. Stephens, J. K. Nørskov, I. Chorkendorff, *Nature* **2019**, *570*, 504.
- [13] R. Shi, Y. Zhao, G. I. N. Waterhouse, S. Zhang, T. Zhang, *ACS Catal.* **2019**, *9*, 9739.
- [14] Q. Qin, T. Heil, M. Antonietti, M. Oschatz, *Small Methods* **2018**, *2*, 1800202.
- [15] J. Zhang, Y. Ji, P. Wang, Q. Shao, Y. Li, X. Huang, *Adv. Funct. Mater.* **2020**, *30*, 1906579.
- [16] L. Zeng, X. Li, S. Chen, J. Wen, F. Rahmati, J. van der Zalm, A. Chen, *Nanoscale* **2020**, *12*, 6029.
- [17] G.-F. Chen, Y. Yuan, H. Jiang, S.-Y. Ren, L.-X. Ding, L. Ma, T. Wu, J. Lu, H. Wang, *Nat. Energy* **2020**, *5*, 605.
- [18] A. Stirling, I. Pápai, J. Mink, D. R. Salahub, *J. Chem. Phys.* **1994**, *100*, 2910.
- [19] R. K. Rai, D. Tyagi, S. K. Singh, *Eur. J. Inorg. Chem.* **2017**, *2017*, 2450.
- [20] S. Xu, D. C. Ashley, H.-Y. Kwon, G. R. Ware, C.-H. Chen, Y. Losovyj, X. Gao, E. Jakubikova, J. M. Smith, *Chem. Sci.* **2018**, *9*, 4950.
- [21] W. Li, C. Xiao, Y. Zhao, Q. Zhao, R. Fan, J. Xue, *Catal. Lett.* **2016**, *146*, 2585.
- [22] T. Wu, X. Kong, S. Tong, Y. Chen, J. Liu, Y. Tang, X. Yang, Y. Chen, P. Wan, *Appl. Surf. Sci.* **2019**, *489*, 321.
- [23] D. Reyter, G. Chamoulaud, D. Bélanger, L. Roué, *J. Electroanal. Chem.* **2006**, *596*, 13.
- [24] Y. Wang, W. Zhou, R. Jia, Y. Yu, B. Zhang, *Angew. Chem., Int. Ed.* **2020**, *59*, 5350.
- [25] Y. Wang, A. Xu, Z. Wang, L. Huang, J. Li, F. Li, J. Wicks, M. Luo, D.-H. Nam, C.-S. Tan, Y. Ding, J. Wu, Y. Lum, C.-T. Dinh, D. Sinton, G. Zheng, E. H. Sargent, *J. Am. Chem. Soc.* **2020**, *142*, 5702.
- [26] L. Su, K. Li, H. Zhang, M. Fan, D. Ying, T. Sun, Y. Wang, J. Jia, *Water Res.* **2017**, *120*, 1.
- [27] J. Gao, B. Jiang, C. Ni, Y. Qi, Y. Zhang, N. Oturan, M. A. Oturan, *Appl. Catal., B* **2019**, *254*, 391.
- [28] C. Li, K. Li, C. Chen, Q. Tang, T. Sun, J. Jia, *Sep. Purif. Technol.* **2020**, *237*, 116485.
- [29] Y. Wang, C. Liu, B. Zhang, Y. Yu, *Sci. China Mater.* **2020**, *63*, 2530.
- [30] G. Wen, J. Liang, Q. Liu, T. Li, X. An, F. Zhang, A. A. Alshehri, K. A. Alzahrani, Y. Luo, Q. Kong, X. Sun, *Nano Res.* **2022**, *15*, 972.
- [31] G. Wen, J. Liang, L. Zhang, T. Li, Q. Liu, X. An, X. Shi, Y. Liu, S. Gao, A. M. Asiri, Y. Luo, Q. Kong, X. Sun, *J. Colloid Interface Sci.* **2022**, *606*, 1055.
- [32] Z.-Y. Wu, M. Karamad, X. Yong, Q. Huang, D. A. Cullen, P. Zhu, C. Xia, Q. Xiao, M. Shakouri, F.-Y. Chen, J. Y. (Timothy) Kim, Y. Xia, K. Heck, Y. Hu, M. S. Wong, Q. Li, I. Gates, S. Siahrostami, H. Wang, *Nat. Commun.* **2021**, *12*, 2870.
- [33] X. Deng, Y. Yang, L. Wang, X.-Z. Fu, J.-L. Luo, X. Deng, L. Wang, -Z. X. Fu, J.-L. Luo, Y. Yang, *Adv. Sci.* **2021**, *8*, 2004523.
- [34] N. C. Kani, J. A. Gauthier, A. Prajapati, J. Edgington, I. Bordawekar, W. Shields, M. Shields, L. C. Seitz, A. R. Singh, M. R. Singh, *Energy Environ. Sci.* **2021**, *14*, 6349.
- [35] M. Ghazouani, H. Akrouf, L. Bousselmi, *Desalin. Water Treat.* **2015**, *53*, 1107.
- [36] J. Ding, W. Li, Q.-L. Zhao, K. Wang, Z. Zheng, Y.-Z. Gao, *Chem. Eng. J.* **2015**, *271*, 252.
- [37] L. Maachou, K. Qi, E. Petit, Z. Qin, Y. Zhang, D. Cot, V. Flaud, C. Reibel, H. El-Maghrbi, L. Li, P. Miele, D. Kaplan, M. Chhowalla, N. Onofrio, D. Voiry, *J. Mater. Chem. A* **2020**, *8*, 25053.
- [38] W. Teng, N. Bai, Y. Liu, Y. Liu, J. Fan, W. X. Zhang, *Environ. Sci. Technol.* **2018**, *52*, 230.
- [39] G. You, C. Wang, J. Hou, P. Wang, Y. Xu, L. Miao, J. Liu, *Chem. Eng. J.* **2021**, *419*, 129646.
- [40] Z. Liu, S. Dong, D. Zou, J. Ding, A. Yu, J. Zhang, C. Shan, G. Gao, B. Pan, *Water Res.* **2020**, *173*, 115596.
- [41] B. L. He, J. S. Shen, Z. X. Tian, *Phys. Chem. Chem. Phys.* **2016**, *18*, 24261.
- [42] D. Liu, J. Li, S. Ding, Z. Lyu, S. Feng, H. Tian, C. Huyan, M. Xu, T. Li, D. Du, P. Liu, M. Shao, Y. Lin, *Small Methods* **2020**, *4*, 1900827.
- [43] C. Zhu, Q. Shi, B. Z. Xu, S. Fu, G. Wan, C. Yang, S. Yao, J. Song, H. Zhou, D. Du, S. P. Beckman, D. Su, Y. Lin, *Adv. Energy Mater.* **2018**, *8*, 1801956.
- [44] M. Xiao, J. Zhu, L. Ma, Z. Jin, J. Ge, X. Deng, Y. Hou, Q. He, J. Li, Q. Jia, S. Mukerjee, R. Yang, Z. Jiang, D. Su, C. Liu, W. Xing, *ACS Catal.* **2018**, *8*, 2824.
- [45] H. Zhang, J. Li, S. Xi, Y. Du, X. Hai, J. Wang, H. Xu, G. Wu, J. Zhang, J. Lu, J. Wang, *Angew. Chem., Int. Ed.* **2019**, *58*, 14871.
- [46] S. Vijay, J. A. Gauthier, H. H. Heenen, V. J. Bukas, H. H. Kristoffersen, K. Chan, *ACS Catal.* **2020**, *10*, 7826.
- [47] F. Lü, S. Zhao, R. Guo, J. He, X. Peng, H. Bao, J. Fu, L. Han, G. Qi, J. Luo, X. Tang, X. Liu, *Nano Energy* **2019**, *61*, 420.
- [48] L. Zhang, M. Cong, X. Ding, Y. Jin, F. Xu, Y. Wang, L. Chen, L. Zhang, *Angew. Chem.* **2020**, *132*, 10980.
- [49] L. Zhang, X. Ji, X. Ren, Y. Ma, X. Shi, Z. Tian, A. M. Asiri, L. Chen, B. Tang, X. Sun, *Adv. Mater.* **2018**, *30*, 1800191.
- [50] J. Yang, A. R. Mohmad, Y. Wang, R. Fullon, X. Song, F. Zhao, I. Bozkurt, M. Augustin, E. J. G. Santos, H. S. Shin, W. Zhang, D. Voiry, H. Y. Jeong, M. Chhowalla, *Nat. Mater.* **2019**, *18*, 1309.
- [51] B. Tang, Z. G. Yu, H. L. Seng, N. Zhang, X. Liu, Y.-W. Zhang, W. Yang, H. Gong, *Nanoscale* **2018**, *10*, 20113.
- [52] M. Li, H. Du, L. Kuai, K. Huang, Y. Xia, B. Geng, *Angew. Chem.* **2017**, *129*, 12823.
- [53] X. Chen, N. C. Berner, C. Backes, G. S. Duesberg, A. R. McDonald, *Angew. Chem., Int. Ed.* **2016**, *55*, 5803.
- [54] Y. Shi, Y. Wang, J. I. Wong, A. Y. S. Tan, C.-L. Hsu, L.-J. Li, Y.-C. Lu, H. Y. Yang, *Sci. Rep.* **2013**, *3*, 2169.
- [55] R. Wang, M. Yan, H. Li, L. Zhang, B. Peng, J. Sun, D. Liu, S. Liu, *Adv. Mater.* **2018**, *30*, 1800618.
- [56] Y. Wang, A. Xu, Z. Wang, L. Huang, J. Li, F. Li, J. Wicks, M. Luo, D. H. Nam, C. S. Tan, Y. Ding, J. Wu, Y. Lum, C. T. Dinh, D. Sinton, G. Zheng, E. H. Sargent, *J. Am. Chem. Soc.* **2020**, *142*, 5702.

- [57] X. Fu, X. Zhao, X. Hu, K. He, Y. Yu, T. Li, Q. Tu, X. Qian, Q. Yue, M. R. Wasielewski, Y. Kang, *Appl. Mater. Today* **2020**, *19*, 100620.
- [58] Y. Wang, W. Zhou, R. Jia, Y. Yu, B. Zhang, *Angew. Chem., Int. Ed.* **2020**, *59*, 5350.
- [59] J. M. McEnaney, S. J. Blair, A. C. Nielander, J. A. Schwalbe, D. M. Koshy, M. Cargnello, T. F. Jaramillo, *ACS Sustainable Chem. Eng.* **2020**, *8*, 2672.
- [60] N. Dubouis, C. Yang, R. Beer, L. Ries, D. Voiry, A. Grimaud, *ACS Catal.* **2018**, *8*, 828.
- [61] T. Yang, T. T. Song, J. Zhou, S. Wang, D. Chi, L. Shen, M. Yang, Y. P. Feng, *Nano Energy* **2020**, *68*, 104304.
- [62] J.-X. Liu, D. Richards, N. Singh, B. R. Goldsmith, *ACS Catal.* **2019**, *9*, 7052.
- [63] G. Li, D. Zhang, Q. Qiao, Y. Yu, D. Peterson, A. Zafar, R. Kumar, S. Curtarolo, F. Hunte, S. Shannon, Y. Zhu, W. Yang, L. Cao, *J. Am. Chem. Soc.* **2016**, *138*, 16632.
- [64] R. Dronskowski, P. E. Blöchl, *J. Phys. Chem.* **1993**, *97*, 8617.
- [65] R. Nelson, C. Ertural, J. George, V. L. Deringer, G. Hautier, R. Dronskowski, *J. Comput. Chem.* **2020**, *41*, 1931.
- [66] L. Jingshan, I. Jeong-Hyeok, M. T. Mayer, S. Marcel, N. Mohammad Khaja, P. Nam-Gyu, T. S. David, F. H. Jin, G. Michael, *Science* **2014**, *345*, 1593.